Journal of Power Sources 344 (2017) 46–55

Contents lists available at ScienceDirect

Journal of Power Sources

journal homepage: www.elsevier.com/locate/jpowsour

Growing large columnar grains of $CH_3NH_3PbI_3$ using the solid-state reaction method enhanced by less-crystallized nanoporous PbI_2 films

Huifeng Zheng [a, b], Weiqi Wang [a, b], Yangqiao Liu [a, c, *], Jing Sun [a, **]

[a] State Key Laboratory of High Performance Ceramics and Superfine Microstructure, Shanghai Institute of Ceramics, Chinese Academy of Sciences, 1295 Dingxi Road, Shanghai 200050, PR China
[b] University of Chinese Academy of Sciences, 19 Yuquan Road, Beijing 100049, PR China
[c] Suzhou Institute of SICCAS (Shanghai Institute of Ceramics, Chinese Academy of Sciences), 238 North Changchun Road, Taicang 215499, Jiangsu Province, PR China

HIGHLIGHTS

- Nanoporous PbI_2 is superior to compact PbI_2 in preparing $CH_3NH_3PbI_3$ films.
- Nanoporous PbI_2 film is critical for growing large columnar grains of $CH_3NH_3PbI_3$.
- Annealing temperature ≥120 °C is also vital to grow large columnar grains.
- A V''_{Pb}-assisted hooping process is proposed to explain the grain growth.

GRAPHICAL ABSTRACT

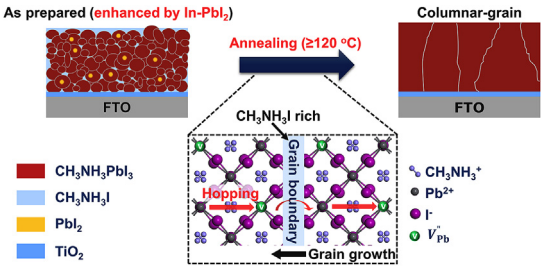

ARTICLE INFO

Article history:
Received 6 November 2016
Received in revised form
6 January 2017
Accepted 25 January 2017
Available online 31 January 2017

Keywords:
Perovskite solar cells
Columnar grains
Grain growth
Solid-state reaction
Nanoporous PbI_2

ABSTRACT

Compact, pinhole-free and PbI_2-free perovskite films, are desirable for high-performance perovskite solar cells (PSCs), especially if large columnar grains are obtained in which the adverse effects of grain boundaries will be minimized. However, the conventional solid-state reaction methods, originated from the two-step method, failed to grow columnar grains of $CH_3NH_3PbI_3$ in a facile way. Here, we demonstrate a strategy for growing large columnar grains of $CH_3NH_3PbI_3$, by less-crystallized nanoporous PbI_2 (ln-PbI_2) film enhanced solid-state reaction method. We demonstrated columnar grains were obtainable only when ln-PbI_2 films were applied. Therefore, the replacement of compact PbI_2 by ln-PbI_2 in the solid-sate reaction, leads to higher power conversion efficiency, better reproducibility, better stability and less hysteresis. Furthermore, by systematically investigating the effects of annealing temperature and duration, we found that an annealing temperature ≥120 °C was also critical for growing columnar grains. With the optimal process, a champion efficiency of 16.4% was obtained and the average efficiency reached 14.2%. Finally, the mechanism of growing columnar grains was investigated, in which a V''_{Pb}-assisted hooping model was proposed. This work reveals the origins of grain growth in the solid-state reaction method, which will contribute to preparing high quality perovskite films with much larger columnar grains.

1. Introduction

Organometal halide perovskite solar cells have risen sharply in the field of photovoltaic research during the past five years, and the

* Corresponding author. State Key Laboratory of High Performance Ceramics and Superfine Microstructure, Shanghai Institute of Ceramics, Chinese Academy of Sciences, 1295 Dingxi Road, Shanghai 200050, PR China.
** Corresponding author.
E-mail addresses: yqliu@mail.sic.ac.cn (Y. Liu), jingsun@mail.sic.ac.cn (J. Sun).

http://dx.doi.org/10.1016/j.jpowsour.2017.01.108
0378-7753/

power conversion efficiency (PCE) has increased dramatically from 9.7% to over 20% [1–5]. The dramatic improvement of PCE mainly lies in the development of preparation methods for fabricating high-quality perovskite films: compact, pinhole-free and PbI_2-free perovskite films [3,6–8]. Among them, the two-step solution deposition method is widely used to prepare perovskite films, because it offers more controllable morphology [3,9,10]. However, the conventional two-step dipping method frequently failed to convert PbI_2 into $CH_3NH_3PbI_3$ effectively in planar perovskite solar cells (PSCs), resulting in a dilemma between the reaction completeness and controllable morphology [11–13]. To solve the problems, some modified editions using solid-state reaction method have been proposed, in which the reaction occurs between PbI_2 film and CH_3NH_3I (MAI) solid rather than MAI solution [14–17].

On the other hand, in order to increase PCE further, trap-states in perovskite films are needed to be eliminated, which lie at surface, grain boundaries and bulk section [18,19]. Among them, grain boundaries are the most obvious ones, as the perovskite films are usually made up of several stacking layers of small grains which are about hundred nanometers [20,21]. The grain boundaries have been directly observed to cause severer nonradiative loss than the bulk section [22]. To overcome the drawbacks of grain boundaries, two strategies are applied: passivating them [18,23,24] or growing larger grains [25,26]. Many reports have shown that perovskite films consisting of larger grains do show much better photovoltaic performance than those with the smaller ones [7,27]. Therefore, growing larger grains is a desirable way to overcome the drawbacks of grain boundaries. Especially, the adverse effect of grain boundaries will be minimized when columnar grains are obtained, in which photocarriers will avoid passing through any additional grain boundaries except those at the interfaces with electron-transporting layer and hole-transporting layer [20,21,28,29].

However, many reports have shown that the conventional solid-state reaction method, driven by medium-high temperature (around 100 °C) thermal annealing, is difficult to grow columnar grains due to the ineffective grain growth of $CH_3NH_3PbI_3$ [21,26,30,31]. Though Ren et al. managed to grow micron-sized grains by elevating the reaction temperature to 200 °C, the PCE is much lower than those prepared at lower temperature reported by others [14,23]. That's probably ascribed to the increase of bulk defects at high temperature [19]. In addition, Huang and his colleagues proposed solvent annealing and non-wetting surface-driven methods to realize significant grain growth [21,26]. However, both of them have some drawbacks. For solvent annealing, CH_3NH_3I-PbI_2-solvent complex (DMF or DMSO) tends to form, which will result in tree-like morphology with many pinholes [32,33]; while for the surface-driven method, effective grain growth is only accessible when hydrophobic substrates are applied. In short, due to the failed grain growth, it's still a challenge to grow large columnar grains of $CH_3NH_3PbI_3$, with the conventional solid-state reaction method at medium-high temperature.

Yang et al. have demonstrated it is critical for grain growth to uniformly disperse excess MAI inside the $CH_3NH_3PbI_3$ (PbI_2) films [34]. However, taking into account the process of conventional solid-state reaction method, MAI is usually stacked on the compact PbI_2 (c-PbI_2) layer, in which MAI can hardly penetrate into the PbI_2 layer. That is the probable reason why conventional solid-state reaction fails to effectively drive grain growth by thermal annealing.

On the other hand, nanoporous PbI_2 (n-PbI_2) films have been demonstrated as an effective way to accelerate the reaction between MAI and PbI_2, by dispersing MAI inside the n-PbI_2 layer to make the reaction happen in the entire thickness simultaneously [12,13,15,35–39]. It indicates that nanoporous PbI_2 films may be an effective way to uniformly disperse MAI inside the entire film of PbI_2, as MAI solution is able to infiltrate into the nanopores quickly by capillary action. However, to our best knowledge, the nanoporous PbI_2 films have never been applied to grow columnar grains of perovskite.

Here, combining the role of excessive MAI playing in grain growth and the function of n-PbI_2 to uniformly disperse MAI inside the entire film, we propose the application of n-PbI_2 in solid-state reaction to facilitate grain growth in order to obtain large columnar grains of $CH_3NH_3PbI_3$. We demonstrate a solid-state reaction method, enhanced by less-crystallized nanoporous PbI_2 (ln-PbI_2) films, is able to grow micron-sized columnar grains. The application of ln-PbI_2 instead of c-PbI_2 leads to acquiring columnar grains, in addition to a faster and more complete conversion into $CH_3NH_3PbI_3$. Therefore, much higher PCE, improved reproducibility and stability were realized, apart from less hysteresis, when ln-PbI_2 was applied. By optimizing the annealing temperature and duration, a champion efficiency of 16.4% was achieved, and the average efficiency reached 14.2%. Finally, the mechanism of growing columnar grains by ln-PbI_2 enhanced solid-state reaction method is discussed, in which we proposed a model of grain growth based on V''_{Pb}-assisted hooping process.

2. Experimental section

2.1. Materials and reagents

CH_3NH_3I was synthesized according to the procedure reported in literature [40]. PbI_2, anhydrous chlorobenzene, Li-bis(trifluoromethanesulfonyl)imide (Li-TFSI) and 4-*tert*-Butylpridine (t-BP) were purchased from Sigma-Aldrich. 2,2′,7,7′-Tetrakis [*N*,*N* -di(4-methoxyphenyl)amino]-9,9′,-spirobifluorene (Spiro-MeOTAD) and Tris(2-(1H -pyrazol-1-yl)-4-*tert*-butylpyridine)-cobalt(III)Tris(bis(trifluoromethylsulfonyl)imide)) (FK209 Co(III) TFSI salt) were purchased from Lumtec, Taiwan. Dimethyl Formamide (DMF) and 2-propanol (IPA) were dehydrated by molecular sieves (4A) before use.

2.2. Device fabrication

Fluorine-doped tin oxide (FTO; 15 Ω sq^{-1}, Nippon Sheet Glass) glass substrates were patterned by Zn powder and diluted HCl solution. The resultant FTO substrates were cleaned sequentially in detergent (Hellmanex II, 2%), water, ethanol, acetone and ethanol with ultrasonication and then treated with ultraviolet (UV) for 15 min. Those cleaned FTO substrates were subsequently coated with a compact TiO_2 layer by spin-coating a yellowish solution of tetrabutyl titanate [41]. After drying at 70 °C, the films were annealed at 500 °C for 30 min. Then, they were treated in 40 mM $TiCl_4$ aqueous solution for 30 min at 70 °C, and rinsed with deionized water and ethanol before being annealed at 500 °C for another 30 min.

After cooling down, the substrates were treated with UV for 15 min again before the deposition of perovskite layer. Then, a layer of PbI_2 was spin-coated (1 M PbI_2 in DMF kept at 70 °C, 3000 r.p.m for 60 s), from which compact PbI_2 (c-PbI_2) films were obtained after drying at 70 °C for 30 min. While for preparing less-crystallized nanoporous PbI_2 (ln-PbI_2) films, antisolvent-solvent extraction process was applied by dispensing IPA on the surface of pristine PbI_2 films and spinning off, as reported in our previous work [37]. To prepare perovskite layer, 8 mg ml^{-1} and 30 mg ml^{-1} MAI solution (in IPA) were sequentially spin-coated on both kinds of PbI_2 films, and perovskite films were obtained by annealing at 100 °C-160 °C for varied duration. While for the interdiffusion method, only 30 mg ml^{-1} MAI solution was spin-coated onto the c-

PbI_2 film. To avoid the decomposition of $CH_3NH_3PbI_3$, the annealing duration was shortened to 20 min and 10 min for 140 °C and 160 °C, respectively.

The hole-transporting layer (HTL) was prepared by spin-coating (4000 r.p.m for 30 s) of a solution of Spiro-MeOTAD (72.3 mg ml^{-1}) with a recipe as reported [3], followed by oxidation in desiccator overnight. Finally, ~100 nm of Ag was evaporated onto the top of HTL, with an effective area of 0.15 cm^2 for device. All the procedures of preparing perovskite layer and HTL were conducted inside an Ar-filled glovebox.

2.3. Measurement and characterization

X-ray diffraction (XRD) was conducted on Rigaku D/max 2550V with Cu Kα radiation at a step size of 0.02°. The absorption spectra of $CH_3NH_3PbI_3$ films were measured by a UV/Vis/NIR spectrophotometer (Lambda 950, Perkin Elmer). A field emission scanning electron microscopy (FESEM; SU8220, Hitachi) was used to investigate the morphology of $CH_3NH_3PbI_3$ films and conduct Energy Dispersive X-Ray Spectroscopy (EDS) test. An atomic force microscope (AFM; ScanAsyst, Veeco Dimension Icon) was used to image the topography and measure surface roughness in the tapping mode. Hall effect measurement was conducted on a physical property measurement system (PPMS-9(dxl), Quantum Design). Fourier transform infrared spectroscopy (FTIR) spectra were recorded on Bruker Tensor 27 spectrophotometer using the standard Pike ATR cell. The *J-V* curves of perovskite solar cells were measured with Keithley 2400 source meter through reverse scan (1 V to −0.1 V) with a step size of 11 mV and delay time of 20 ms, under the simulated AM 1.5G illumination (100 mW cm^{-2}; Oriel Sol3A Class AAA Solar Simulator, Newport) which had been calibrated by an optical power meter (Newport, 1918-R). And the measurement was conducted at room temperature under controlled humidity of 20% RH. Incident photon-to-electron conversion efficiency (IPCE) spectra were characterized by an IPCE test system (Zahner, CIMPS-pcs2/IPCE). Open-circuit photovoltage decay (OCVD) and electrochemical impedance spectroscopy (EIS) were measured by an electrochemical workstation (CHI660D, CH Instruments) under simulated AM 1.5G illumination (100 mW cm^{-2}), and the EIS were performed in the frequency range from 1 MHz to 1 HZ, by applying a bias voltage of its corresponding V_{oc}.

3. Results and discussion

3.1. The advantages of ln-PbI_2 over c-PbI_2

Fig. 1a presents the procedures for preparing different types of PbI_2 films and the distinct morphology of the corresponding PbI_2 films. C-PbI_2 films were prepared in the conventional method, in which films were annealed directly after the spin-coating of PbI_2 solution. The less-crystallized nanoporous PbI_2 films were prepared in a facile way developed by our group, called antisolvent-solvent extraction [37], and the annealing process was omitted. The omission of annealing leads to a much worse crystallinity but similar morphology compared to that with annealing; however, it results in a faster conversion into perovskite (Figs. S1a–c) [42]. The subtle differences in the preparation procedure led to distinct morphology, as shown in the SEM images of Fig. 1a. C-PbI_2 film is totally compact, while ln-PbI_2 film is nanoporous. The forming mechanism of nanoporous morphology has been detailedly studied in our previous work [37].

Although both types of PbI_2 films deliver the same characteristic peaks of PbI_2, the crystallinity of c-PbI_2 films is much better than that of ln-PbI_2 films (Fig. 1b and c). However, as Ko et al. indicated, the improved crystallinity of PbI_2 film would retard the conversion of PbI_2 into $CH_3NH_3PbI_3$ [42]. We compared the evolution of absorbance at 750 nm with the extension of loading time, from which the conversion rate could be compared qualitatively. Fig. S1c shows that the absorbance increases more sharply for ln-PbI_2 than c-PbI_2, which can be ascribed to the synergic effect of nanoporous morphology of PbI_2 film and it worse crystallinity [12,13,38,42]. It

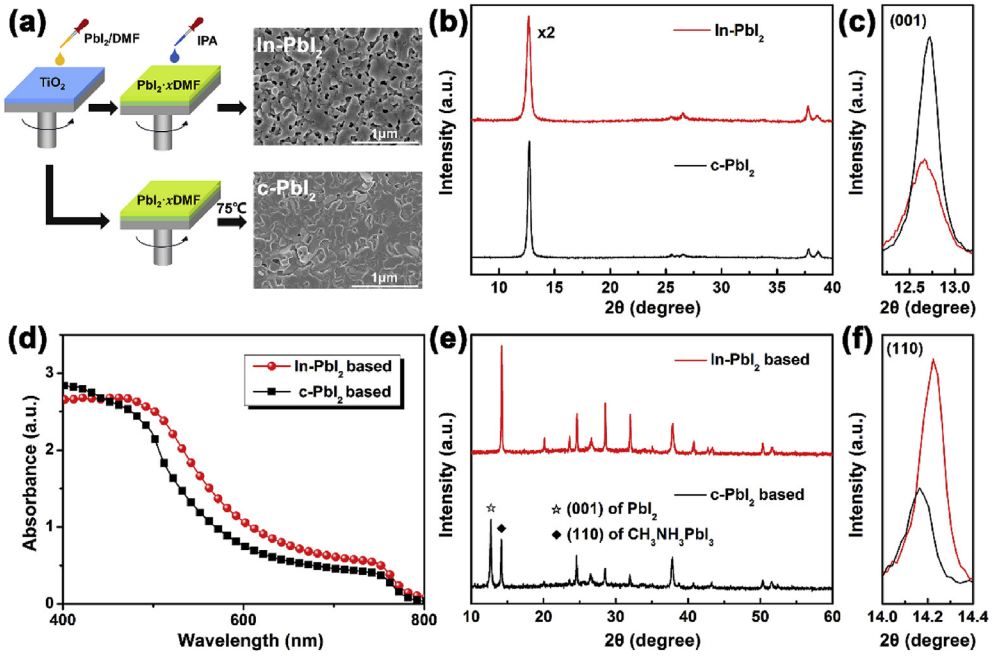

Fig. 1. Differences between c-PbI_2 and ln-PbI_2 films. (a) The preparation procedures and distinct morphology, (b) XRD spectra and (c) the comparison of the (001) peak of different types of PbI_2 films. (d) UV–vis absorption spectra, (e) XRD spectra and (f) the comparison of the (110) peak of $CH_3NH_3PbI_3$ based on different types of PbI_2 films. All the perovskite films were annealed for 30 min at 120 °C.

demonstrates the advantage of applying ln-PbI_2 to prepare perovskite films.

$CH_3NH_3PbI_3$ films were prepared with the solid-state reaction method [15,43], by sequentially spin-coating of 8 mg ml^{-1} and 30 mg ml^{-1} MAI solution onto the PbI_2 films and annealing. It's worth noting that the combination of low and high concentration of MAI is indispensable to obtain PbI_2-free $CH_3NH_3PbI_3$ films in our case, as indicated by Fig. S1d. The resultant $CH_3NH_3PbI_3$ films, based on different types of PbI_2, were characterized by UV–vis spectrophotometer. As shown in Fig. 1d, the c-PbI_2 based perovskite film exhibits much lower absorbance than that based on ln-PbI_2, which can be inferred from the photographs in Fig. S1e as well. The lower absorbance of the c-PbI_2 based one mainly comes from the incomplete conversion of PbI_2 into $CH_3NH_3PbI_3$, confirmed by the XRD characterization in Fig. 1e and f. As the XRD spectra show, the (001) peak of PbI_2 (near 12.7°) is strong in the c-PbI_2 based one, indicating the incomplete conversion of PbI_2 into $CH_3NH_3PbI_3$; contrastively, the characteristic peak of PbI_2 is absent in the perovskite film based on ln-PbI_2. One thing is worth noting: the remnant PbI_2 in the c-PbI_2 based perovskite film (Fig. 1e) is actually much less than the $CH_3NH_3PbI_3$ phase, as much higher intensity of PbI_2 is expected than the same quantity of $CH_3NH_3PbI_3$, which has been reported [3,44].

Moreover, the morphology of perovskite films based on different types of PbI_2 were compared. As Fig. 2a–b shows, both films are compact and pinhole-free consisting of polycrystals, but the grain size varies significantly. The average grain size is 135 nm and 222 nm for c-PbI_2 and ln-PbI_2 based perovskite films (Fig. S2), respectively. In addition, all the perovskite films are smooth, exhibiting mirror effect in photographs, as shown in Fig. S1e. Meanwhile, the cross-sectional morphology varies widely as well, as presented in Fig. 2c–d. For the c-PbI_2 based sample, the film is made up of several stacking layers of small grains; while for the ln-PbI_2 based one, the film mainly consists of columnar grains whose sizes are as large as the film's thickness. Columnar grains, connecting the cathode and anode directly, were demonstrated to be beneficial for high photovoltaic performance by reducing recombination at grain boundaries [20,21]. In addition, some residual PbI_2 nanoplates are present between $CH_3NH_3PbI_3$ and TiO_2 layer in the c-PbI_2 based perovskite film, which were verified by the EDS test (Figs. S3a and b). That was reported to inhibit electron transfer from perovskite into TiO_2 layer [13]. To exclude the possibility that the deficiency of MAI leads to the absence of columnar grains in the c-PbI_2 based one, we prepared perovskite film with a lower spin speed for MAI solution, by which more MAI would be deposited on the c-PbI_2 layer. As displayed in Fig. S3c, with more MAI deposited on the surface of PbI_2 layer, the columnar grains are still absent though some large grains (~500 nm) appear in the upper layer near the surface. It suggests that nanoporous PbI_2 is indispensable to grow columnar grains of $CH_3NH_3PbI_3$ with the conventional solid-state reaction method at medium-high temperature. Moreover, it's worth noting that our ln-PbI_2-assisted method differs much from other porous-PbI_2-assisted methods: firstly, the perovskite film prepared with our method, consists of large columnar grains, which has never been reported by other porous-PbI_2-assisted methods; secondly, here, we adopted the solid-state reaction method, which is more controllable than the conventional two-step dipping method utilized by most reports.

Then, those perovskite films based on different types of PbI_2, were fabricated into planar perovskite solar cells with a setup of FTO/compact TiO_2/$CH_3NH_3PbI_3$/Spiro-MeOTAD/Ag. The comparison of photovoltaic performance is shown in Fig. 2e. Ln-PbI_2 based samples deliver the best efficiency of 15.9%, much better than its counterpart based on c-PbI_2 which only shows 12.9%. However, in consideration of significant PbI_2 remained, the PCE of c-PbI_2 based PSC is surprisingly high, which mainly comes from two reasons: firstly, the residue of PbI_2 is much lesser than it seems, as indicated previously; secondly, the remnant PbI_2 does not form a continuous layer, alleviating the drawbacks of PbI_2. Specifically, short-circuit current density (J_{SC}) and open-circuit voltage (V_{OC}) of the c-PbI_2 based sample are only slightly lower than that of ln-PbI_2 based one,

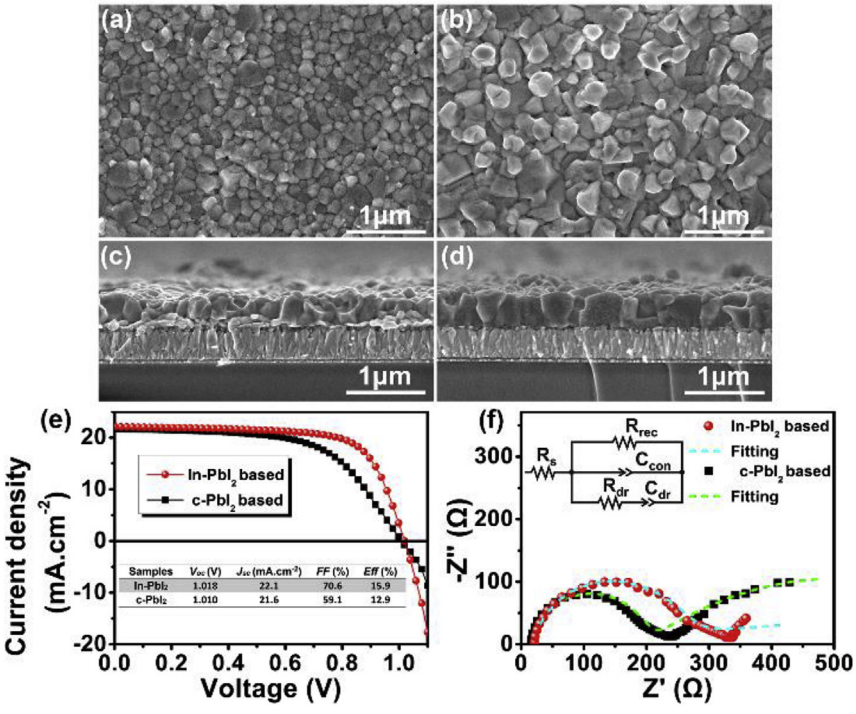

Fig. 2. SEM images of $CH_3NH_3PbI_3$ films based on (a) (c) c-PbI_2, (b) (d) ln-PbI_2. (e) The *J-V* curves and (f) the corresponding Nyquist plots at $V = V_{oc}$ of the best samples based on different types of PbI_2 under the illumination of AM 1.5G (100 mW cm^{-2}).

while the greatest difference lies in fill factor (*FF*). For c-PbI_2 based sample, *FF* was only 59%, about 17% relatively lower than that of ln-PbI_2 based one. The lower *FF* suggests severer recombination in the c-PbI_2 based perovskite film, which mainly results from the inhibited injection of electron by the remnant PbI_2 [13]. That was confirmed by the electrochemical impedance spectrum (EIS) measurement, displayed in Fig. 2f. EIS is a tool widely used in PSCs, however, there are some discrepancies in the models of interpretation [12,45]. Cheng and his colleagues have systematically investigated the EIS of planar PSCs, and proposed a more suitable model for planar setup, in which the high-frequency features were attributed to charge recombination across the perovskite/contact interfaces [45,46]. As shown in Fig. 2f, the recombination resistance of c-PbI_2 based sample (0.8 kΩ) is much smaller than that of ln-PbI_2 based one (1.6 kΩ), indicating a severer interfacial recombination in the case of c-PbI_2. That has been confirmed by open-circuit photovoltage decay (OCVD) test as well (Fig. S4). OCVD is a facile technique to measuring carrier lifetime in solar cells, widely used in dye-sensitized solar cells and PSCs [25,47,48]. The lifetime of ln-PbI_2 based device is significantly longer than that of c-PbI_2 based one (Fig. S4), indicating a severer recombination in the case of c-PbI_2. It can be ascribed to two factors: firstly, the remnant PbI_2 has a much higher trap density than perovskite, which will cause severe recombination [49]; secondly, the recombination is enhanced by the fact that the injection of electrons from perovskite to TiO_2 is inhibited by the PbI_2 interlayer [13].

Additionally, the distributions of photovoltaic parameters are compared (Fig. S5), from which we can conclude all the parameters are much lower and more scattered for the c-PbI_2 based ones than those based on ln-PbI_2. That can be attributed to the uncontrollable remnant PbI_2, as suggested by Han's group [11]. Moreover, we also compared the stability of PSCs based on those two types of PbI_2 (relative humidity ~30%, 27 °C). As depicted in Fig. S6, the PSC based on ln-PbI_2 was able to maintain 90% of the primary PCE when stored for 9 days; while that based on c-PbI_2 completely failed during the same period. It demonstrates the superior stability of the ln-PbI_2 based PSCs compared with the c-PbI_2 based ones, which mainly comes from two reasons: the larger grain size [50] and the elimination of remnant PbI_2 in the case of ln-PbI_2 based device [13,38,51]. Furthermore, the PSC based on ln-PbI_2 deliver smaller hysteresis than that of the c-PbI_2 based one, as depicted in Fig. S7. That can also be ascribed to the large grain size (fewer grain boundaries) in the case of ln-PbI_2 based sample, as a faster ion migration is found at grain boundaries than that in grain interiors which is responsible for the hysteresis in PSCs [52].

In short, ln-PbI_2 is superior to c-PbI_2 when applied in the solid-state reaction: Firstly, annealing is not necessary for ln-PbI_2, which is more energy saving; Secondly, ln-PbI_2 can convert into perovskite much faster and more completely. Moreover, the replacement of c-PbI_2 by ln-PbI_2 leads to the presence of large columnar grains, in stark contrast to those stacking layers of small grains in the case of c-PbI_2. Therefore, the application of ln-PbI_2 results in not only much higher PCE but also an improved reproducibility and stability.

3.2. The effects of annealing temperature and duration

Aforementioned results demonstrate that columnar grains are obtainable even with thermal annealing at medium-high temperature (120 °C), when ln-PbI_2 films are applied; however, the origin of growing columnar grains is still not understood. Therefore, the effects of annealing temperature and duration on the film's morphology and properties were systematically investigated.

As shown in top-view SEM images Fig. 3a–d, grain growth in plane is not remarkable below 160 °C, while many micron-sized

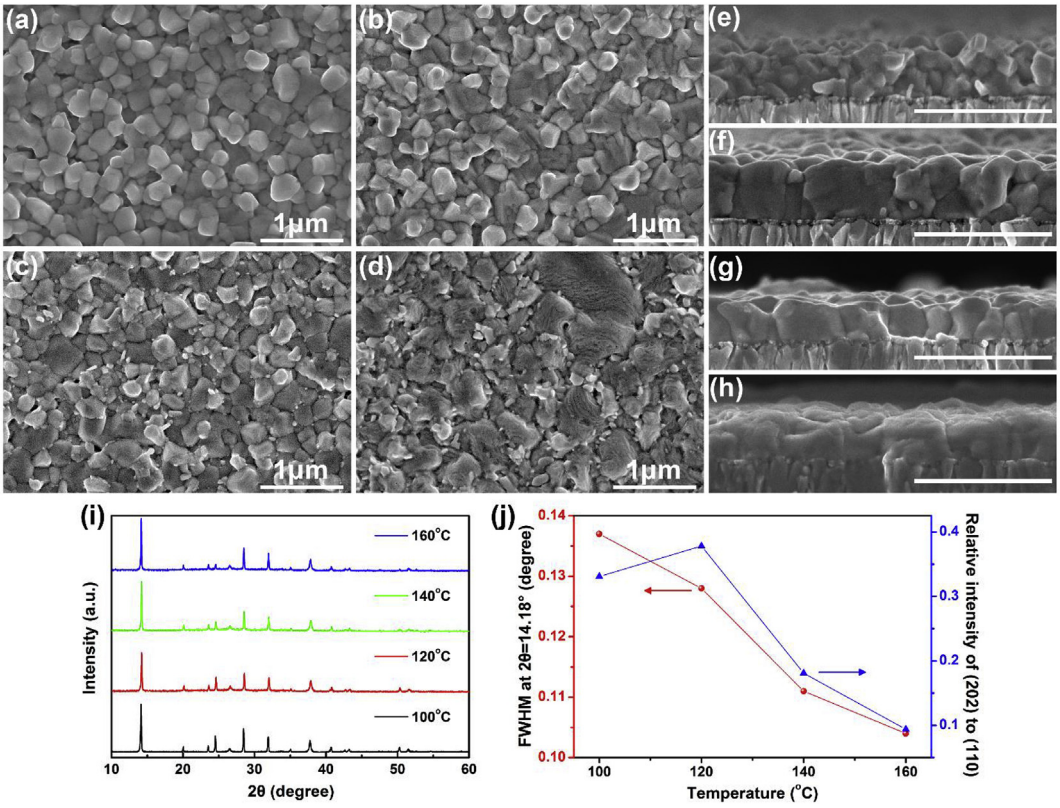

Fig. 3. SEM images of perovskite films annealed at different temperatures: (a) (e) 100 °C, (b) (f) 120 °C, (c) (g) 140 °C, (d) (h) 160 °C. The scale bars is 1 μm. (i) XRD spectra and (j) the corresponding films' full width at half maximum (FWHM) of the (110) peak and the ratio of (202) peak to (110) peak varying with the annealing temperature.

grains appear when annealed at 160 °C. Specifically, as shown in Figs. S2b and S8, the average grain size is 197 nm, 222 nm, 270 nm and 479 nm for 100 °C, 120 °C, 140 °C and 160 °C, respectively. In addition, some tiny particles, with relatively bright contrast compared with adjacent grains, are present at the grain boundaries when annealed above 140 °C (including 140 °C), which are speculated to be PbI_2 resulting from the decomposition of perovskite at high temperature, as reported by others [53,54]. Moreover, many tiny pinholes appear in the film annealed at 160 °C, which probably come from the decomposition of perovskite as well, as displayed in Fig. S9. To characterize the roughness of those perovskite films, AFM tests were conducted (Fig. S10). The result implies that the reaction temperature has little effect on the Root-mean-square (RMS) roughness of perovskite films [25], though annealing at 120 °C results in the smoothest film with a RMS of 44.8 nm. On the other hand, grain growth is apparent in the thickness direction. As shown in Fig. 3e, when prepared at 100 °C, the perovskite layer is made up of several stacking layers of small grains; however, those small grains grow into columnar grains when the annealing temperature increases to 120 °C (Fig. 3f). Further elevating the temperature to 140 °C does not see significant changes, except that the proportion of columnar grains increases, displayed in Fig. 3g. When the annealing temperature further increases to 160 °C, the vertical grain boundaries of columnar grains are obscure (Fig. 3h), indicating that the grains are sintered together [55].

In addition, XRD measurement of these films, prepared at varied annealing temperatures, was carried out in order to confirm their phase composition. Fig. 3i shows all the samples display the same characteristic peaks, with 14.22°, 20.15°, 23.61° and 24.62° assigned to the (110), (200), (211) and (202) crystal planes of $CH_3NH_3PbI_3$ (tetragonal phase), respectively [56]. Luckily, as shown in Fig. 3i, all the films annealed at different temperatures seem PbI_2-free; however, due to the detection limit of XRD characterization, the presence of trace amount of PbI_2 can't be excluded absolutely, as indicated by those tiny bright particles in Fig. 3c and d. In addition, the relative intensity of (202) peak to (110) peak reduces as the annealing temperature increases, except at 120 °C where it increases a little, as shown in Fig. 3j. That means annealing at higher temperature will lead to more consistently oriented grains. Moreover, the full width at half maximum (FWHM) of perovskite's (110) peak decreases gradually from 0.137° to 0.104° when the annealing temperature increases from 100 °C to 160 °C, which mainly results from the reduction of grain boundaries.

Surprisingly, the FWHM of our perovskite films annealed for 30 min at 100 °C, is much narrower than the reported one, which is over 0.2° when annealing for 1 h at 105 °C by the interdiffusion method [30]. The narrower FWHM means better crystallinity, which may come from reduction in bulk defects or grain boundaries [30]. As the grain sizes are similar in both cases [30], the higher crystallinity probably indicates fewer bulk defect in our films. As indicated by previous studies, the bulk defects mainly result from non-stoichiometrical composition [57–59]. That may suggest the perovskite films in our case are closer to the stoichiometrical composition than those prepared with the interdiffusion method [30], which was verified by the EDS test (displayed in Fig. S11). It can be attributed to the facilitation of reaction and homogenization by nanoporous PbI_2, because MAI is more evenly distributed inside the nanopores in our case; while for the interdiffusion method, MAI layer is stacked on the compact PbI_2 layer, in which homogenization is more difficult. It shows the advantages of ln-PbI_2 over c-PbI_2 again.

Furthermore, we compared the absorbance of perovskite films prepared at varied annealing temperatures, presented in Fig. 4a. It shows that the samples of 100 °C and 120 °C show the highest and lowest absorbance (above 500 nm), respectively; while those of

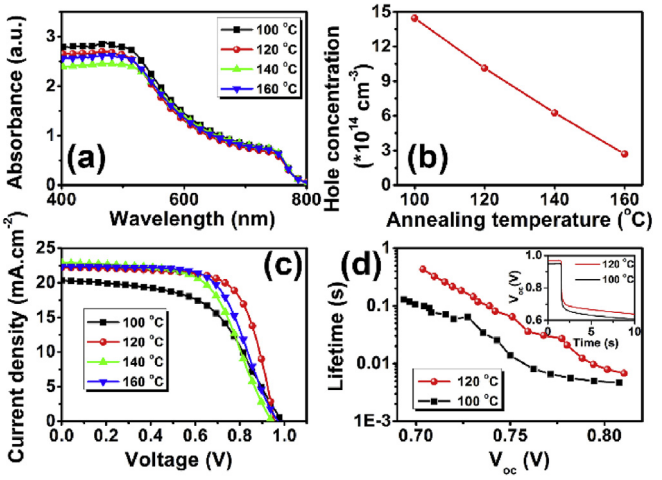

Fig. 4. Effects of annealing temperature on (a) UV–vis spectra, (b) carrier concentration. (c) *J-V* curves of perovskite films with varied annealing temperature, and the *J-V* curves are from the best samples in the same batch. (d) Comparison of carrier lifetime of samples prepared at 100 °C and 120 °C. The inset of (d) are the OCVD curves, from which the carrier lifetimes are deduced.

140 °C and 160 °C are similar. The variation of absorbance with annealing temperature mainly comes from the change of roughness, as a smooth surface will reduce light trapping effect, shown in Fig. S10 [60]. Nevertheless, the light-harvesting efficiency (LHE) doesn't vary much (Fig. S12a), which will not affect the J_{sc} apparently. Moreover, Hall effect measurement was conducted in order to study the influence of annealing temperature on carrier concentration. As reported by others, all the samples prepared with the solid-state reaction method are p-type, probably resulting from Pb vacancies [30,57,58]. Fig. 4b shows the hole concentration decreases from 14.5 × 10^{14} cm^{-3} to 2.7 × 10^{14} cm^{-3} for films with annealing temperature rising from 100 °C to 160 °C. The reduction of hole concentration can be ascribed to the decrease of defects: fewer atomic vacancies (Pb) by eliminating excessive MAI and fewer grain boundaries resulting from grain growth [30].

To investigate the effects of annealing temperature on photovoltaic performance, we fabricated planar PSCs with the setup previously mentioned. Fig. 4c compares the *J-V* curves of the best samples in the same batch, based on different annealing temperatures. When the annealing temperature increases from 100 °C to 120 °C, both of J_{sc} and *FF* increase from 20.4 mA cm^{-2} to 22.2 mA cm^{-2} and 54%–69.5%, respectively. The increase of J_{sc} (from 100 °C to 120 °C) was verified by the IPCE test as well, shown in Fig. S12b. It shows that the IPCE of 120 °C is apparently higher than that of 100 °C in the entire range, resulting in the integrated J_{sc} of 21.2 mA cm^{-2} (120 °C) and 19.5 mA cm^{-2} (100 °C) which agree well with the measured ones from the *J-V* curves. The improvement of J_{sc} and *FF* can be ascribed to the reduction of grain boundaries parallel to the substrate. As shown in Fig. 3(e) and (f), with

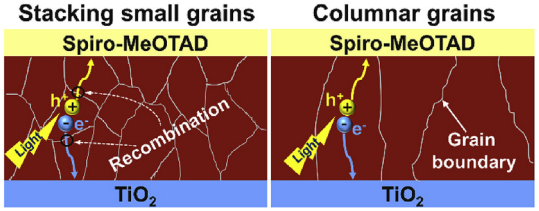

Fig. 5. Schematic illustration of photocarriers transporting in the setup of stacking small grains and columnar grains, respectively. In the former setup, photocarriers have to pass through additional grain boundaries which cause severe recombination.

columnar grains in case of 120 °C, the photocarriers will avoid passing through several layers of grain boundaries which cause severe recombination, as they do in the case of 100 °C (as depicted in Fig. 5) [20,21]. That was confirmed by the OCVD test. As the inset of Fig. 4d shows, V_{oc} decays faster for the sample prepared at 100 °C than that of 120 °C, indicating shorter carrier lifetime in small grains (100 °C) than columnar grains (120 °C). As depicted in Fig. 4d, the carrier lifetime of columnar grains (120 °C) is over 2 times longer than that of small grains (100 °C). Therefore a higher charge collection efficiency is expected in the sample of 120 °C than that of the 100 °C based sample, which contributes to a higher J_{sc} at 120 °C [61]. That demonstrates the advantage of columnar grains.

Further raising the annealing temperature leads to a significant loss in *FF*, from 69.5% at 120 °C to 60.0%, 63.1% for 140 °C and 160 °C, respectively. Meanwhile, J_{sc} remains almost unchanged with value above 22 mA cm^{-2}; while for V_{oc}, it changes from 0.954 V to 0.940 V and 0.970 V for 140 °C and 160 °C, as shown in Table S1. As a result, the champion efficiency decreases from 14.7% at 120 °C to 12.8%, 13.7% for 140 °C and 160 °C, respectively. The deterioration of performance at 140 °C, compared with 120 °C, mainly comes from the enhanced recombination by PbI_2 particles at the grain boundaries on the surface (Fig. 3c) [62]; while the improvement at 160 °C, with respect to 140 °C, may result from the reduction of grain boundaries by sintering grains together (Fig. 3h), which remedies the influence of remnant PbI_2 [55]. In addition, the average performance of perovskite films prepared at varied temperature are also listed in Table S1, from which we can infer that 120 °C is the optimum annealing temperature for the ln-PbI_2 enhanced solid-state reaction method.

Furthermore, the annealing duration at 120 °C was optimized as well. The photovoltaic performance of samples with varied annealing duration is displayed in Fig. 6. Specifically, J_{sc} remains almost unchanged, around 22 mA cm^{-2} for all the samples. While for the average V_{oc} and *FF*, both of them peak at 60 min. As a result, the samples annealed for 60 min deliver the highest average PCE of 14.6%. The increase of photovoltaic performance when extending duration from 30 min to 60 min can be ascribed to the reduction of defects by grain growth (Fig. 3b and f, S2b, S13a, c and e), during which many grains grow to micron-size; while it declines when further extending to 120 min, which may come from the decomposition of perovskite films, as indicated by those tiny particles at grain boundaries (Fig. S13b), though no detectable PbI_2 is present (Fig. S13g). In addition, the performance of samples annealed for 60 min display the smallest standard deviation, as listed in Table S2. Hence, annealing for 60 min at 120 °C is the optimum preparation process.

One thing is worth noting: thermal annealing with a temperature ≥120 °C is indispensable for growing columnar grains in our method, which provides the driving force for grain boundary migration. That was easily demonstrated by characterizing the evolution of grain growth at 100 °C for varied annealing duration, presented in Fig. 3a, e and Fig. S14. As shown in Fig. 3a and S14a, the average grain size almost remains unchanged, varying from 197 nm to 199 nm as the annealing duration (at 100 °C) increases from 30 min to 120 min. In addition, the grain growth is not apparent in the thickness direction either, without any columnar grains present, shown in Fig. S14b.

The typical setup of planar PSC with the optimal process is displayed in Fig. 7a, in which the perovskite layer is about 360 nm in thickness with tiny variation. The uniformity in thickness contributes to the high photovoltaic performance and reproducibility [6]. Fig. 7b shows the *J-V* curves of the champion device, annealed for 60 min at 120 °C, under forward and reverse scan directions. The reverse scan results in a PCE of 16.4%, higher than 13.6% under forward scan, displaying apparent hysteresis. Moreover, the PCE is independent of scan rate when changing the dwell time from 10 ms to 200 ms, though it drops a bit at 400 ms (Fig. S15). This phenomenon of scan direction-dependent and rate-dependent PCE is frequently reported in perovskite solar cells, which is still an open question [63,64]. In addition, the IPCE spectrum of the champion sample is presented in Fig. 7c. The IPCE curve shows a strong response in the range from 410 nm to 710 nm with efficiency over 80%, and peaks at 91.5% (at 612 nm). The integrated J_{sc} reaches at 21.7 mA cm^{-2}, agreeing well with that measured from the *J-V* curve (22.7 mA cm^{-2}).

In order to evaluate the performance of PSCs more precisely, we also provided the stabilized PCE of a device with top PCE close to the champion device, as displayed in Fig. S16. When held at a forward bias at 0.78 V under AM1.5G illumination, the sample delivers a stabilized photocurrent density of 18.2 mA cm^{-2} and the steady-state PCE reaches 14.2% which is close to the average PCE of that under reverse scan (16.0%) and forward scan (12.9%). Moreover, the PCE distribution of PSCs prepared with the optimal process (annealed for 60 min at 120 °C) is displayed in Fig. 7d, with an

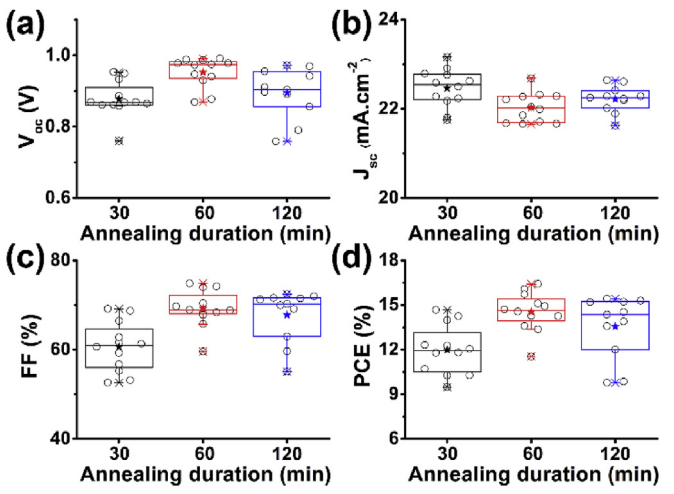

Fig. 6. Effects of annealing duration at 120 °C on the photovoltaic performance: (a) V_{oc}, (b) J_{sc}, (c) *FF*, (d) PCE. Solid stars represent mean values, while hollow circles are raw data.

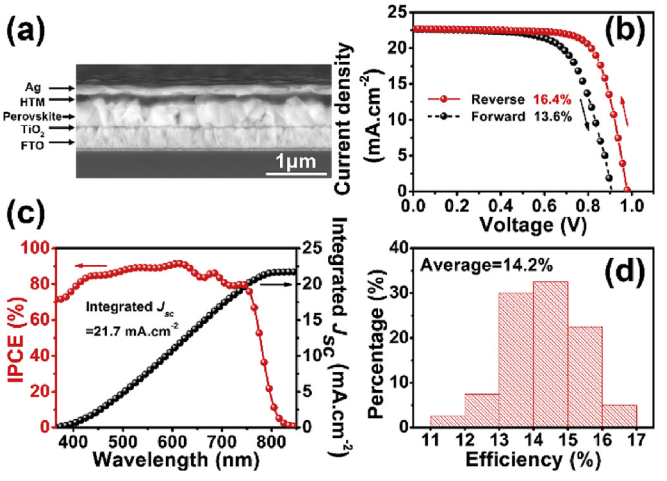

Fig. 7. (a) Setup of planar PSCs in which the perovskite layer was prepared with the optimal process. (b) *J-V* curves of the best sample depending on scanning direction. (c) IPCE and the corresponding integrated J_{sc} of the best sample. (d) Statistics on power conversion efficiency based on the optimum process (120 °C × 60 min, 40 devices).

average efficiency of 14.2% and standard deviation of 1.1%. It shows the desirable reproducibility of the ln-PbI_2 enhanced solid-state reaction method.

3.3. The mechanism of ln-PbI_2 enhanced solid-state reaction

Based on aforementioned results, we can conclude that two factors are critical to grow columnar grains of $CH_3NH_3PbI_3$: the nanoporous morphology of PbI_2 films and thermal annealing with a temperature ≥120 °C. In order to further understand the mechanism of grain growth in the thickness direction, both of XRD spectra and cross-sectional morphology were characterized in the different stages of preparation.

Fig. 8a shows the XRD patterns of perovskite films in the different stages of preparation. For the as prepared one without any annealing, surprisingly, only a bit of PbI_2 remains, indicated by the weak (001) peak of PbI_2. With low-temperature drying, PbI_2-free perovskite films are obtained. Additionally, (110) peak of perovskite gets stronger (Fig. 8b), indicating better crystallinity. When annealed at medium-high temperature (120 °C) further, the crystallinity of perovskite films is enhanced significantly, suggested by the dramatically increased (110) peak. Meanwhile, the FHWM of (110) peak decreases sharply from 0.254° (as prepared one) to 0.137° (annealed for 60 min at 120 °C), demonstrating a considerable improvement in crystallinity as well. Two things are worth noting: Firstly, excessive MAI is believed to remain in both of the as prepare perovskite film and that with low-temperature drying, though lack of characteristic peak near 30° in XRD spectra [8,65]. It may come from the low crystallinity of MAI in the films, as indicated by Yang et al. [34]. Additionally, that was supported by both of SEM characterization and Fourier transform infrared spectroscopy test, in which excessive MAI is observed both in the as prepared one and that with low-temperature drying (Fig. S17). Secondly, we succeed to prepare PbI_2-free perovskite films even with low-temperature solid-state reaction, which is desirable for flexible perovskite solar cells. Relevant work about more detailed studies is under preparation.

Moreover, the evolution of cross-sectional morphology was also observed as the preparation went on, as shown in Fig. 8c–e. For the as prepared one, the film consists of several stacking layers of small grains whose sizes are smaller than 100 nm. In addition, the film is not compact in the upper part, as displayed in Fig. 8c. After drying at 75 °C for 5 min, the morphology changes apparently (Fig. 8d), indicated by the larger grain size (typically >100 nm), and the film get much more compact than the as prepared one. With medium-high temperature annealing further, many columnar grains are present (Fig. 8e), which implies significant grain growth is driven by the thermal annealing at medium-high temperature.

Finally, based on those analyses, we propose the mechanism of growing columnar grains in the ln-PbI_2 enhanced solid-state reaction, as schematically shown in Fig. 8f. The entire preparation consists of 4 stages and 3 steps. Stage 1 is the as prepared ln-PbI_2 film, which turns into the as prepared perovskite film (stage 2) by spin-coating of MAI solution. As analyzed above, some PbI_2 and excessive MAI remain, though the main phase is perovskite (Fig. 8a and Fig. S17). Additionally, the residual MAI is supposed to distribute in the entire thickness rather than on the surface only, which has been demonstrated crucial for grain growth [34], because MAI solution manages to infiltrate nanoporous PbI_2 effectively [15]. After low-temperature drying (75 °C), more compact perovskite films with small grains are obtained, and the remnant PbI_2 is eliminated while the excessive MAI still remains (stage 3). With further annealing at medium-high temperature (≥ 120 °C), the small grains grow into columnar grains with larger size,

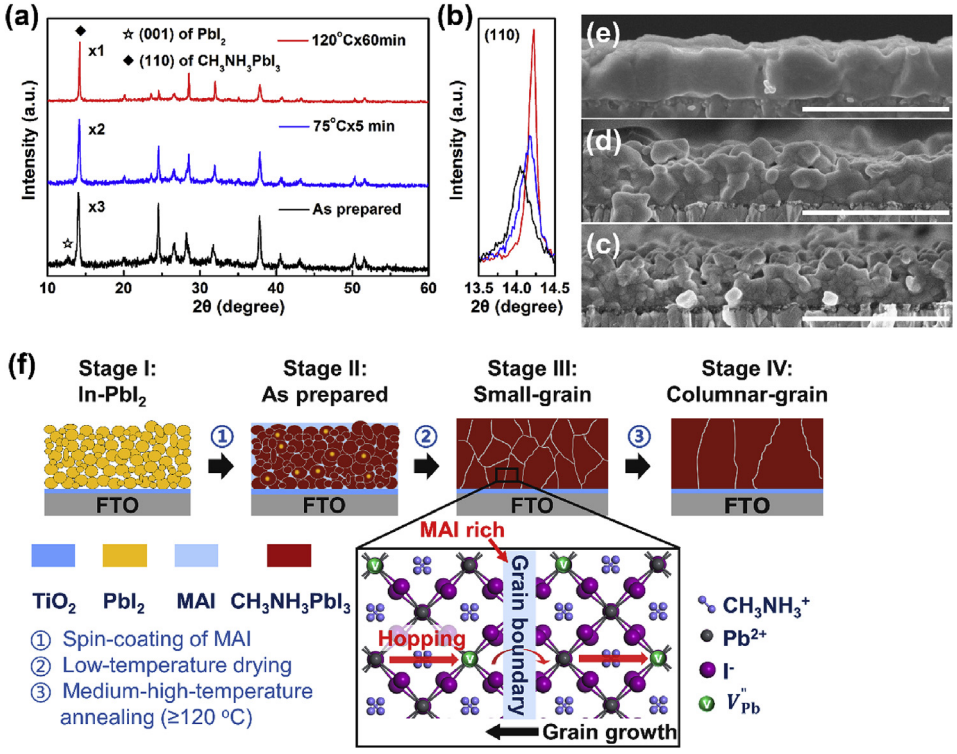

Fig. 8. The evolution of XRD spectra (a) (b) and cross-sectional morphology (c–e) of perovskite films at different stages of preparation: (c) as prepared, (d) after drying (75 °C × 5 min), (e) after annealing (120 °C × 60 min). The scale bars is 1 μm. (f) Schematic illustration of preparation mechanism of ln-PbI_2 assisted solid-state reaction. As $CH_3NH_3^+$ is reorienting quasi-randomly at room temperature, it's unrealistic to distinguish between C and N [66,67]. Therefore, $CH_3NH_3^+$ is presented in a brief way.

and the crystallinity of perovskite films get much better (stage 4).

To explain the role of excessive MAI playing in grain growth, we propose a $V_{Pb}^{''}$-assisted grain growth model. Based on the classical grain growth model, for ionic compound (just as $CH_3NH_3PbI_3$), grain boundary migration is realized by the diffusion of ions, which diffuses by hooping between vacancies of ions or interstitial sites while grain boundary moves in the reverse direction [68,69]. In our case, the most possible point defect is $V_{Pb}^{''}$ because CH_3NH_3I is much richer than PbI_2, agreeing with the previous Hall effect result (Fig. 4b) [57–59]. As indicated by some reports, however, the activation energy for Pb^{2+} migration is much higher than that of I^- and $CH_3NH_3^+$, which is likely to be the rate controlling process of grain growth [70,71]. That would be the probable reason why a temperature $\geq$120 °C is indispensable for growing columnar grains. Additionally, much more excessive MAI is speculated to be present at grain boundaries in the case of ln-PbI_2 based perovskite films than those based on c-PbI_2. Therefore, more $V_{Pb}^{''}$ are expected to generate near grain boundaries in the case of ln-PbI_2 than that of c-PbI_2, by which the migration rate of grain boundary is significantly accelerated as the grain boundary mobility is proportion to the vacancy concentration [68]. On the other hand, with much richer MAI distributed at grain boundaries in the case of ln-PbI_2 based one, the section near grain boundaries are more disordered, namely in a high-energy state, which may contribute to decreasing the activation energy for Pb^{2+} migration. As a result, the rate of grain growth in the case of ln-PbI_2 based one is much higher than that of the c-PbI_2 based one, leading to large columnar grains in ln-PbI_2 based one while stacking layers of small grains in the c-PbI_2 based one.

4. Conclusion

We demonstrated a strategy to grow high-quality perovskite films with large columnar grains, using the solid-state reaction enhanced by less-crystallized nanoporous PbI_2 films. The results indicate that the ln-PbI_2 films outperform the c-PbI_2 ones when applied in the solid-state reaction, mainly in three aspects: firstly, ln-PbI_2 can convert into perovskite much faster and completely; secondly, larger columnar grains replace the small grains in the case of c-PbI_2; thirdly, the preparation of ln-PbI_2 films is annealing-free, which is more energy-saving. As a result, when c-PbI_2 is replaced by ln-PbI_2 applied in the solid-state reaction, great improvements in PCE, reproducibility and stability are observed. Furthermore, we thoroughly investigated the effects of annealing temperature and duration on the properties and performances of perovskite films, during which the preparation process was optimized as annealing for 60 min at 120 °C. With this optimal process, a champion efficiency of 16.4% was obtained, and the average efficiency reached 14.2%. Finally, the mechanism of growing columnar grains by ln-PbI_2 enhanced solid-state reaction was proposed, in which two factors are crucial: Firstly, thermal annealing with a temperature $\geq$120 °C is needed to provide sufficient driving force for grain growth; Secondly, the uniform distribution of MAI inside nanoporous PbI_2 films, facilitates the migration of grain boundaries by a $V_{Pb}^{''}$-assisted hooping process. This method can be generalized to prepare other organometal halide perovskite films with columnar grains. Moreover, this work sheds light on the origins of grain growth in the solid-state reaction method, which can be applied to prepare perovskite films with much larger grains.

Acknowledgments

This work was supported by the National Basic Research Program of China (2012CB932303), the National Natural Science Foundation of China (Grant No. 61574148, 51272265), Taicang Key R&D Projects (TC2016SF09) and the State Key Laboratory for Modification of Chemical Fibers and Polymer Materials, Donghua University (No. LK1517).

Appendix A. Supplementary data

Supplementary data related to this article can be found at http://dx.doi.org/10.1016/j.jpowsour.2017.01.108.

References

[1] H. Kim, C. Lee, J. Im, K. Lee, T. Moehl, A. Marchioro, S. Moon, R. Humphry-Baker, J. Yum, J.E. Moser, M. Gratzel, N. Park, Sci. Rep. 2 (2012) 591.
[2] M.M. Lee, J. Teuscher, T. Miyasaka, T.N. Murakami, H.J. Snaith, Science 338 (2012) 643–647.
[3] J. Burschka, N. Pellet, S. Moon, R. Humphry-Baker, P. Gao, M.K. Nazeeruddin, M. Gratzel, Nature 499 (2013) 316–319.
[4] W.S. Yang, J.H. Noh, N.J. Jeon, Y.C. Kim, S. Ryu, J. Seo, S.I. Seok, Science 348 (2015) 1234–1237.
[5] D. Bi, W. Tress, M.I. Dar, P. Gao, J. Luo, C. Renevier, K. Schenk, A. Abate, F. Giordano, J.P. Correa Baena, J.D. Decoppet, S.M. Zakeeruddin, M.K. Nazeeruddin, M. Gratzel, A. Hagfeldt, Sci. Adv. 2 (2016) e1501170.
[6] M. Liu, M.B. Johnston, H.J. Snaith, Nature 501 (2013) 395–398.
[7] W. Nie, H. Tsai, R. Asadpour, J.C. Blancon, A.J. Neukirch, G. Gupta, J.J. Crochet, M. Chhowalla, S. Tretiak, M.A. Alam, H.L. Wang, A.D. Mohite, Science 347 (2015) 522–525.
[8] N.J. Jeon, J.H. Noh, Y.C. Kim, W.S. Yang, S. Ryu, S. Il Seok, Nat. Mater. 13 (2014) 897–903.
[9] J. Im, H. Kim, N. Park, APL Mater. 2 (2014) 81510.
[10] N. Yantara, D. Sabba, F. Yanan, J.M. Kadro, T. Moehl, P.P. Boix, S. Mhaisalkar, M. Gratzel, C. Gratzel, Chem. Commun. 51 (2015) 4603–4606.
[11] Y. Wu, A. Islam, X. Yang, C. Qin, J. Liu, K. Zhang, W. Peng, L. Han, Energy Environ. Sci. 7 (2014) 2934–2938.
[12] T. Liu, Q. Hu, J. Wu, K. Chen, L. Zhao, F. Liu, C. Wang, H. Lu, S. Jia, T. Russell, R. Zhu, Q. Gong, Adv. Energy Mater. 6 (2016) 1501890.
[13] H. Zhang, J. Mao, H. He, D. Zhang, H.L. Zhu, F. Xie, K.S. Wong, M. Gratzel, W.C.H. Choy, Adv. Energy Mater. 5 (2015) 1501354.
[14] Z. Xiao, C. Bi, Y. Shao, Q. Dong, Q. Wang, Y. Yuan, C. Wang, Y. Gao, J. Huang, Energy Environ. Sci. 7 (2014) 2619–2623.
[15] Y. Zhou, M. Yang, A.L. Vasiliev, H.F. Garces, Y. Zhao, D. Wang, S. Pang, K. Zhu, N.P. Padture, J. Mater. Chem. A 3 (2015) 9249–9256.
[16] L. Chen, F. Tang, Y. Wang, S. Gao, W. Cao, J. Cai, L. Chen, Nano Res. 8 (2015) 263–270.
[17] Z. Yang, B. Cai, B. Zhou, T. Yao, W. Yu, S.F. Liu, W. Zhang, C. Li, Nano Energy 15 (2015) 670–678.
[18] Y. Shao, Z. Xiao, C. Bi, Y. Yuan, J. Huang, Nat. Commun. 5 (2014) 5784.
[19] W. Peng, B. Anand, L. Liu, S. Sampat, B.E. Bearden, A.V. Malko, Y.J. Chabal, Nanoscale 8 (2016) 1627–1634.
[20] L. Huang, Z. Hu, G. Yue, J. Liu, X. Cui, J. Zhang, Y. Zhu, Phys. Chem. Chem. Phys. 17 (2015) 22015–22022.
[21] Z. Xiao, Q. Dong, C. Bi, Y. Shao, Y. Yuan, J. Huang, Adv. Mater. 26 (2014) 6503–6509.
[22] D.W. de Quilettes, S.M. Vorpahl, S.D. Stranks, H. Nagaoka, G.E. Eperon, M.E. Ziffer, H.J. Snaith, D.S. Ginger, Science 348 (2015) 683–686.
[23] B. Yang, O. Dyck, J. Poplawsky, J. Keum, A. Puretzky, S. Das, I. Ivanov, C. Rouleau, G. Duscher, D. Geohegan, K. Xiao, J. Am. Chem. Soc. 137 (2015) 9210–9213.
[24] D. Son, J. Lee, Y.J. Choi, I. Jang, S. Lee, P.J. Yoo, H. Shin, N. Ahn, M. Choi, D. Kim, N. Park, Nat. Energy 1 (2016) 16081.
[25] X. Ren, Z. Yang, D. Yang, X. Zhang, D. Cui, Y. Liu, Q. Wei, H. Fan, S.F. Liu, Nanoscale 8 (2016) 3816–3822.
[26] C. Bi, Q. Wang, Y. Shao, Y. Yuan, Z. Xiao, J. Huang, Nat. Commun. 6 (2015) 7747.
[27] H.D. Kim, H. Ohkita, H. Benten, S. Ito, Adv. Mater. 28 (2016) 917–922.
[28] M. Xiao, F. Huang, W. Huang, Y. Dkhissi, Y. Zhu, J. Etheridge, A. Gray-Weale, U. Bach, Y. Cheng, L. Spiccia, Angew. Chem. Int. Ed. 126 (2014) 10056–10061.
[29] F. Zhang, J. Song, L. Zhang, F. Niu, Y. Hao, P. Zeng, H. Niu, J. Huang, J. Lian, J. Mater. Chem. A 4 (2016) 8554–8561.
[30] C. Bi, Y. Shao, Y. Yuan, Z. Xiao, C. Wang, Y. Gao, J. Huang, J. Mater. Chem. A 2 (2014) 18508–18514.
[31] Q. Dong, Y. Yuan, Y. Shao, Y. Fang, Q. Wang, J. Huang, Energy Environ. Sci. 8 (2015) 2464–2470.
[32] S. Bae, S.J. Han, T.J. Shin, W.H. Jo, J. Mater. Chem. A 3 (2015) 23964–23972.
[33] F. Hao, C.C. Stoumpos, Z. Liu, R.P.H. Chang, M.G. Kanatzidis, J. Am. Chem. Soc. 136 (2014) 16411–16419.
[34] M. Yang, Y. Zhou, Y. Zeng, C. Jiang, N.P. Padture, K. Zhu, Adv. Mater. 27 (2015) 6363–6370.
[35] Y. Shi, X. Wang, H. Zhang, B. Li, H. Lu, T. Ma, C. Hao, J. Mater. Chem. A 3 (2015) 22191–22198.
[36] M.I. El-Henawey, R.S. Gebhardt, M.M. El-Tonsy, S. Chaudhary, J. Mater. Chem. A 4 (2016) 1947–1952.

[37] H. Zheng, W. Wang, S. Yang, Y. Liu, J. Sun, RSC Adv. 6 (2016) 1611–1617.
[38] J. Cao, F. Wang, H. Yu, Y. Zhou, H. Lu, N. Zhao, C. Wong, J. Mater. Chem. A 4 (2016) 10223–10230.
[39] Y. Zhao, K. Zhu, J. Mater. Chem. A 3 (2015) 9086–9091.
[40] Q. Chen, H. Zhou, Z. Hong, S. Luo, H. Duan, H. Wang, Y. Liu, G. Li, Y. Yang, J. Am. Chem. Soc. 136 (2014) 622–625.
[41] H. Xue, X. Kong, Z. Liu, C. Liu, J. Zhou, W. Chen, S. Ruan, Q. Xu, Appl. Phys. Lett. 90 (2007) 201118.
[42] H. Ko, J. Lee, N. Park, J. Mater. Chem. A 3 (2015) 8808–8815.
[43] G. Li, K.L. Ching, J.Y.L. Ho, M. Wong, H. Kwok, Adv. Energy Mater. 5 (2015) 1401775.
[44] D.H. Cao, C.C. Stoumpos, C.D. Malliakas, M.J. Katz, O.K. Farha, J.T. Hupp, M.G. Kanatzidis, APL Mater. 2 (2014) 91101.
[45] A.R. Pascoe, N.W. Duffy, A.D. Scully, F. Huang, Y. Cheng, J. Phys. Chem. C 119 (2015) 4444–4453.
[46] G.A. Sepalage, S. Meyer, A. Pascoe, A.D. Scully, F. Huang, U. Bach, Y. Cheng, L. Spiccia, Adv. Funct. Mater. 25 (2015) 5650–5661.
[47] A. Zaban, M. Greenshtein, J. Bisquert, ChemPhysChem 4 (2003) 859–864.
[48] W. Ke, G. Fang, J. Wan, H. Tao, Q. Liu, L. Xiong, P. Qin, J. Wang, H. Lei, G. Yang, M. Qin, X. Zhao, Y. Yan, Nat. Commun. 6 (2015) 6700.
[49] Y. Zhao, A.M. Nardes, K. Zhu, Faraday Discuss. 176 (2014) 301–312.
[50] C. Chiang, C. Wu, ChemSusChem 9 (2016) 2666–2672.
[51] F. Liu, Q. Dong, M.K. Wong, A.B. Djurišić, A. Ng, Z. Ren, Q. Shen, C. Surya, W.K. Chan, J. Wang, A.M.C. Ng, C. Liao, H. Li, K. Shih, C. Wei, H. Su, J. Dai, Adv. Energy Mater 6 (2016) 1502206.
[52] Y. Shao, Y. Fang, T. Li, Q. Wang, Q. Dong, Energy Environ. Sci. 9 (2016) 1752–1759.
[53] Q. Chen, H. Zhou, T. Song, S. Luo, Z. Hong, H. Duan, L. Dou, Y. Liu, Y. Yang, Nano Lett. 14 (2014) 4158–4163.
[54] T. Zhang, N. Guo, G. Li, X. Qian, Y. Zhao, Nano Energy 26 (2016) 50–56.
[55] B.E. Cohen, S. Gamliel, L. Etgara, APL Mater. 2 (2014) 81502.
[56] T. Baikie, Y. Fang, J.M. Kadro, M. Schreyer, F. Wei, S.G. Mhaisalkar, M. Gratzel, T.J. White, J. Mater. Chem. A 1 (2013) 5628–5641.
[57] W. Yin, T. Shi, Y. Yan, Appl. Phys. Lett. 104 (2014) 63903.
[58] J. Kim, S. Lee, J.H. Lee, K. Hong, J. Phys. Chem. Lett. 5 (2014) 1312–1317.
[59] Q. Wang, Y. Shao, H. Xie, L. Lyu, X. Liu, Y. Gao, J. Huang, Appl. Phys. Lett. 105 (2014) 163508.
[60] L. Zheng, Y. Ma, S. Chu, S. Wang, B. Qu, L. Xiao, Z. Chen, Q. Gong, Z. Wu, X. Hou, Nanoscale 6 (2014) 8171–8176.
[61] A. Hagfeldt, G. Boschloo, L. Sun, L. Kloo, H. Pettersson, Chem. Rev. 110 (2010) 6595–6663.
[62] H. Xu, Y. Wu, J. Cui, C. Ni, F. Xu, J. Cai, F. Hong, Z. Fang, W. Wang, J. Zhu, L. Wang, R. Xu, F. Xu, Phys. Chem. Chem. Phys. 18 (2016) 18607–18613.
[63] H.J. Snaith, A. Abate, J.M. Ball, G.E. Eperon, T. Leijtens, N.K. Noel, S.D. Stranks, J.T. Wang, K. Wojciechowski, W. Zhang, J. Phys. Chem. Lett. 5 (2014) 1511–1515.
[64] H. Chen, N. Sakai, M. Ikegami, T. Miyasaka, J. Phys. Chem. Lett. 6 (2015) 164–169.
[65] Z. Song, S.C. Watthage, A.B. Phillips, B.L. Tompkins, R.J. Ellingson, M.J. Heben, Chem. Mater. 27 (2015) 4612–4619.
[66] A. Mattoni, A. Filippetti, M.I. Saba, P. Delugas, J. Phys. Chem. C 119 (2015) 17421–17428.
[67] R.E. Wasylishen, O. Knop, J.B. Macdonald, Solid State Commun. 56 (1985) 581–582.
[68] L.A.B. Mora, 2D and 3D Grain Growth Modeling and Simulation, RWTH Aachen University, Aachen, 2008.
[69] S.L. Kang, Sintering: Densification, Grain Growth and Microstructure, first ed., Butterworth-Heinemann, Oxford, 2005.
[70] C. Eames, J.M. Frost, P.R.F. Barnes, B.C. O Regan, A. Walsh, M.S. Islam, Nat. Commun. 6 (2015) 7497.
[71] J.M. Azpiroz, E. Mosconi, J. Bisquert, F. De Angelis, Energy Environ. Sci. 8 (2015) 2118–2127.